NASA/CR-1998-206914

Microstructural Characterization of Aluminum-Lithium Alloys 1460 and 2195

Z. M. Wang and R. N. Shenoy
Analytical Services & Materials, Inc., Hampton, Virginia

February 1998

TABLE OF CONTENTS

LIST OF TABLES

LIST OF FIGURES

Microstructural Characterization of Aluminum-Lithium Alloys 1460 and 2195 *

Z.M. Wang and R.N. Shenoy

Analytical Services & Materials, Inc., 107 Research Dr., Hampton, VA 23666

Abstract

Transmission electron microscopy (TEM) and differential scanning calorimetry (DSC) techniques were employed to characterize the precipitate distributions in lithium-containing aluminum alloys 1460 and 2195 in the T8 condition. TEM examinations revealed δ' and T_1 as the primary strengthening precipitates in alloys 1460 and 2195 respectively. TEM results showed a close similarity of the Russian alloy 1460 to the U.S. alloy 2090, which has a similar composition and heat treatment schedule. DSC analyses also indicate a comparable δ' volume fraction. TEM study of a fractured tensile sample of alloy 1460 showed that δ' precipitates are sheared by dislocations during plastic deformation and that intense stress fields arise at grain boundaries due to planar slip. Differences in fracture toughness of alloys 1460 and 2195 are rationalized on the basis of a literature review and observations from the present study.

1. Introduction

Aluminum-Lithium alloys 1460 and 2195 have beneficial combinations of high strength and low density and are being considered for cryogenic tank applications on future launch vehicles. The improved specific properties of these alloys with respect to more conventional materials such as alloy 2219 offer the potential for considerable vehicle weight reduction. Cryogenic tanks are typically integrally stiffened structures produced by costly machining operations from plate. Recently, there has been considerable interest in the use of near-net-shape extrusions as an economical replacement for machined plates. Structure-property studies of candidate alloys in these product forms are needed for design evaluations.

In the present investigation, the skin portions of the integrally stiffened extrusions of the alloys 1460 and 2195 have been evaluated in the T8 condition (artificial aging after 3% stretching). Alloy 1460, especially in the T8 temper, exhibits much lower levels of toughness and yield strength as compared to alloy 2195. Alloy 1460 is very similar to the well-studied alloy 2090 [1,2,3,4] in both mechanical behavior and chemical composition (Table 1) except for a minor alloy addition of Sc to alloy 1460. In view of this, a microstructural characterization of alloy 2090 (artificial aging after 6% stretching) was included for comparison. Fracture toughness and yield strength data for the three alloys are listed in Table 2 [5].

Sc in alloy 1460 increases the number density of δ' precipitates and improves the uniformity of their distribution [6]. Also, Sc has been claimed [7,8] to be very effective in improving the mechanical properties of Al alloys through precipitation of Al_3Sc ($L1_2$) phase [9]. The Al_3Sc dispersion of fine spherical particles increases strength, strongly stabilizes the substructure, and inhibits recrystallization [10, 11, 12].

The aim of the present work is to describe the type, distribution and precipitation sequences of the strengthening phases in these alloys by TEM and DSC analyses; and to

apply this understanding to the interpretation of fracture toughness characteristics. The strengthening mechanisms in the alloys will be discussed in relation to the existing literature as well as the results from the present study.

Table 1. Chemical compositions of alloys 2090, 1460 and 2195 (wt%)

Alloy	Cu	Li	Ag	Mg	Zr	Zn	Sc	Al
2090	2.72	2.07	-	-	0.12	-		balance
1460	2.91	2.14	-	0.003	0.11	-	0.044	balance
2195	4.22	0.98	0.46	0.44	0.12	0.02	-	balance

Table 2. Room temperature fracture toughness and yield strength of near-net-shape extruded Al - Li panels

Alloy	Fracture Toughness, K_{IIC} (MPa $\sqrt{m}$)	Yield Strength, σ_y (MPa)
2090	~ 13	~ 508
1460	~ 20	~ 490
2195	~ 60	~ 550

2. Experimental Procedure

Specimens for microstructural examination of alloys 1460, 2090, and 2195 in the T8 condition, were prepared as ST sections (normal to the extrusion direction) from compact tension (CT) samples machined from the skin region of the extruded panels. In addition, a fractured tensile sample of alloy 1460, aged for 20 hours at 160°C, was examined by TEM to study dislocation-precipitate interactions. The aging conditions studied by TEM are shown in Table 3.

Table 3. Heat treatment conditions for TEM samples of alloys 2090, 1460 and 2195

Alloy	Condition
2090	aged for 30 hours at 160°C
1460	aged for 20 hours at 160°C
2195	aged for 15 hours at 149°C

TEM foils were prepared by standard techniques. The 3 mm discs were abraded using SiC papers to approximately 100 μm thickness, and electropolished in a Tenupol-3 twin

jet electropolisher with a 3:1 methanol:nitric acid electrolyte cooled to a temperature below -20°C. A potential of 12 ±1V was used. All foils were examined in a Philips EM-420T transmission electron microscope. The δ' and T_1 precipitates were examined using centered dark-field (CDF) imaging from (100) superlattice reflections for δ' and reflections intermediate to multiples of Al (111) reflections for T_1.

DSC analyses were performed on the alloy samples (~ 4.5 mm square, 1.5 mm thick and weighing ~80 mg) in flowing dry N_2, using a Thermal Analysis Instruments 2910 apparatus. Alloy conditions for DSC analyses were as follows: alloy 2090 (aged at 160°C for 30 hours); alloy 1460 (aged at 160°C for 16, 20, and 24 hours); and alloy 2195 (aged at 149°C for 10, 15, and 20 hours). Scanning rates of 5, 10, and 20°C/min were employed to examine the kinetics of phase transitions.

3. Results and Discussion

Experimental results from the current study are presented, discussed and compared with previously reported results from the open literature in the following pages. Section 3.1 presents a TEM study of the microstructure and precipitate phases of alloys 1460, 2090 and 2195. Section 3.2 pertains to DSC characterization to define microstructural evolution with aging. Section 3.3 provides a discussion of the toughness behavior of alloys 1460 and 2195 in relation to the microstructural evolution and the influence of precipitate types on the deformation modes.

3.1. TEM Evaluation

3.1.1. Alloys 1460 and 2090

Figures 1 (a) and (b) are low magnification bright field (BF) images of the alloys 1460 and 2090, showing grain shapes and their relative orientation with respect to the short (S) and long transverse (L) directions. Both alloys have comparable grain sizes and primarily unrecrystallized grain structures. The selected area diffraction (SAD) patterns for [001], [101] and [112] zone axes, shown in Figure 2, reveal the presence of δ' (Al_3Li),

β'(Al$_3$Zr) or Al$_3$Sc, T$_1$ (Al$_2$CuLi), θ' (Al$_2$Cu), and Ω (Al$_2$Cu) precipitate phases in the two alloys. Figures 3.1-3.3 present schematics of the indexed SAD patterns corresponding to those in Figure 2. Of the various precipitate diffraction spots, those of δ' appear to be the most intense. This implies that δ' is the most abundant precipitate, and probably the primary strengthening phase in the two alloys. δ' has an L1$_2$ ordered structure, a spherical morphology, is fully coherent with the matrix and has a very small misfit. The L1$_2$ structure results in superlattice reflections (100) and (110). Information on the various phases commonly occurring in Al-Li-Cu alloys is presented in Table 4.

The δ' - CDF images in Figures 4 (a) and 4 (b) indicate that for an identical aging treatment such as 20 hours at 160°C, the general features of δ' particle size, number density and distribution are very similar in both alloys. Additionally, δ' is seen to nucleate not only within the Al matrix but also on the interfaces of θ', Al$_3$Sc, and Al$_3$Zr precipitates. A comparison of Figures 4 (a) and 4 (b) shows that the average size of δ' is slightly smaller in alloy 1460 than in alloy 2090. This may be the result of decreased δ' growth rate in the presence of Sc in alloy 1460 [6]. T$_1$ number densities in both alloys are lower than those of δ', and this is evident in the T$_1$ - CDF images in Figures 5 (a) and 5 (b).

Table 4. Descriptions of various phases in Al-Li-Cu alloys

Precipitate	Structure	Morphology	Habit Plane	Reference
δ' (Al$_3$Li)	L1$_2$	sphere	------	Williams and Edington [13]
θ' (Al$_2$Cu)	tetragonal	Disc	{ 1 0 0 }	Kang and Grant [14]
T$_1$ (Al$_2$Cu Li)	hexagonal	Platelet	{ 1 1 1 }	Huang and Ardell [15]
Ω (Al$_2$Cu)	orthorhombic	Platelet	{ 1 1 1 }	Knowles and Stobbs [16]
S' (Al$_2$CuMg)	orthorhombic	Lath	{ 2 1 0 }	Gupta, Gaunt and Chaturvedi [17]
β' (Al$_3$Zr)	L1$_2$	sphere	------	Huang and Ardell [15]
Al$_3$Sc	L1$_2$	sphere	------	Blake and Hopkins [9]

3.1.2 Alloy 2195

Figure 6 is a low magnification BF image of alloy 2195 where a primarily unrecrystallized grain structure is observed. It is apparent that the average grain/subgrain size is larger in 2195 than in the other alloys (see Figures 1 (a) and 1 (b)). The [100], [101] and [112] SAD patterns shown in Figure 7 clearly reveal the presence of $\delta'(Al_3Li)$, $\beta'(Al_3Zr)$, T_1 (Al_2CuLi) and θ' (Al_2Cu) phases, and the possible presence of Ω (Al_2Cu) and S' (Al_2CuMg) phases. Schematics of the indexed SAD patterns indicating the presence of the above phases were shown in Figures 3.1-3.3. T_1 is the predominant precipitate phase and produces the strongest reflection spots or streaks (Figure 7). According to previous work [18,19], T_1 has a hexagonal crystal structure with an orientation relationship of $(0001)_{T1}$ ‖ $\{111\}_{Al}$ and $<1010>_{T1}$ ‖ $<110>_{Al}$ and a platelet morphology. There are four variants of the T_1 phase which produce four spots in the [001] zone SAD pattern at 1/2[110], 3/2[110], 1/2[-110], and 3/2 [-110]. In the [101] zone SAD pattern, two variants of T_1 are inclined to the zone axis and produce spots at 1/3[220] and 2/3[220]; the other two variants are parallel to the zone axis and produce streaks along the [111] direction. Figures 8 (a) and 8 (b) are BF and CDF images showing a uniform distribution of T_1 within the Al matrix. Precipitation of T_1 on a sub-boundary can also be seen. It is also apparent that T_1 is finer in alloy 2195 than in alloys 1460 or 2090 (see Figure 5). The [001] SAD pattern in Figure 7 showing streaking along the [200] direction reveals the presence of only one variant of θ', which is indicative of strong texturing in the extruded product form [26].

3.2. DSC Evaluation

Differential scanning calorimetry (DSC) is a widely used thermoanalytical tool for microstructural characterization of age hardenable aluminum alloys [20]. The scope of DSC pertinent to the present study includes correlation of microstructural evolution with heat treatment practices; quantitation of precipitate volume fraction and particle size; and analyses of precipitation and dissolution reaction kinetics. The use of DSC, in conjunction

with TEM, can provide a rapid and comprehensive description of the microstructural characteristics of a material.

3.2.1. Alloys 1460 and 2090

a. Identification of the δ' endotherm

Barring minor differences, which are probably related to differences in actual chemistries, the alloys 1460 and 2090 register similar DSC signatures (Figure 9) in a scan from room temperature (RT) to 550°C. The starting microstructures of the aged alloys were dominated by δ' with interspersions of T_1 (see Figures 2, 4 and 5). In these conditions, a 20°C/min DSC scan for the alloys showed a prominent endotherm spanning ~150°C to ~300°C. TEM can be used for the identification of microstructural changes associated with such thermal events. The above endotherm was identified in the following manner as that due to the dissolution of δ'. Samples of alloy 1460 (aged 20h/160°C) and alloy 2090 (aged 30h/160°C) were individually heated at a slow scanning rate (5°C/min) in the DSC cell up to a temperature of ~245°C, corresponding almost to the end of the dissolution endotherm, and were liquid N_2 quenched. The quenched samples were then subjected to TEM analysis. The scanning rate was selected to facilitate attainment of near-equilibrium conditions in the quenched sample. Figures 10 (a) and 10 (b) which typify the microstructures corresponding to this quenched state indicate almost total absence of δ', thus unequivocally identifying the endotherm with δ' dissolution.

b. Volume fraction of δ'

The area under the above endotherm is a direct measure of δ' volume fraction. Volume fraction of a strengthening precipitate is a critical parameter governing material strength and toughness. For the two alloys 2090 and 1460, in the aforementioned heat treated conditions, the δ' volume fraction is essentially the same, as attested to by the similar areas under the curves: 11.2 and 10.9 J/g respectively. The actual value of δ' volume fraction in the microstructure may be estimated from the following formula [21]:

$$V_f = M_p(\rho_s/\rho_p)(A/H_p)$$

Where V_f = volume fraction of δ'; M_p = gram molecular weight of δ'; ρ_s and ρ_p are densities of alloy and δ' respectively [g/cm^3]; A = area under the curve, [J/g]; H_p = molar enthalpy of δ' dissolution, [J].

For a sample calculation, substituting values such as, M_p = 87.885 g /mol; ρ_s = 2.7 to 2.8 g/cm^3; ρ_p = 2.26 g/cm^3; A= 11.2 J/g; and H_p = 11.3 kJ/mol [22], to the above equation gives V_f = 10.6 ± 0.2%. Furthermore, a mass balance calculation indicates that if all the Li in the alloy forms δ', V_f = 31.3%. This clearly implies that Li in excess of that necessary to form 10.6% δ' in the alloy, is available for forming a mixture of Li-rich solid solution and T_1 precipitate. Such calculations provide volume fraction estimations of precipitates, and thus provide a check on the accuracy of any subsequent TEM quantitative analyses of these phases. For example, TEM quantitative analysis of δ' volume fraction in the present study yields V_f of 7.2% for alloy 2090 and 7.9% for alloy 1460, values which are slightly lower than the DSC-derived value of 10.6%. The lower estimates from TEM analysis stem from the fact that the overlapping δ' particles in the foil samples are difficult to account for. Similar TEM estimation errors have been reported earlier for alloy 8090 [23].

c. Effects of aging time on δ' in alloy 1460

Figure 11 shows the effects of aging time at 160°C on the area under the curve and the peak temperature of the δ' endotherm. The peak temperature corresponds to the maximum reaction rate, and is a sensitive measure of average precipitate size. The coarser the δ' resulting from a given aging treatment, the higher the peak temperature.

Little differences exist in volume fraction and average δ' precipitate size for the aging times of 16 and 20 hours. For example, while the start and end temperatures of the δ' endotherm for both 16 and 20 hours aging conditions are 157°C and 262°C, respectively, the peak temperatures are 228°C and 229°C. Concomitantly, volume fraction (as measured by area under the δ' endotherm) is essentially constant at 10.9 J/g. The start temperature of the endotherm corresponds to the dissolution of very fine δ' precipitates; and the end

8

temperature to the coarse δ'. The above values of start, peak, and end temperatures imply the size distribution of δ' precipitates is substantially unaltered while the aging time is increased from 16 hours to 20 hours. For the 24 hours aging condition, however, there appears to be measurable coarsening of δ' without a change in volume fraction. This is indicated by start, peak, and end temperatures rising to 163°C, 234.2°C, and 266°C respectively, with the volume fraction staying constant with the area under the δ' endotherm =10.9 J/g. The δ' coarsening during the progression of aging from 20 to 24 hours thus represents Ostwald ripening.

The above analysis of the effects of aging time on particle size and volume fraction of δ' indicates that optimum strengthening should occur during 16 to 20 hours of aging at 160°C. Aging for longer times is expected to lead to appreciable δ' coarsening and consequent property degradation.

d. Kinetics of δ' dissolution in alloy 1460

In view of almost one-to-one correspondence between the DSC traces for the aging conditions of 24h at 160°C for 1460 and 30h at 160°C for 2090 (see Figure 9), it was deemed appropriate to gather kinetics information on the δ' dissolution for only one of the alloys, namely 1460. Dependence of the δ' endothermic peak temperature on the imposed heating rate in the DSC was documented for three different scanning rates: 5,10, and 20°C/min. Figure 12 is a Kissinger plot [24] of $\ln{(T_m^2/\Phi)}$ versus $1/T_m$, where T_m = peak temperature [K] and Φ = heating rate [°C/s]. The slope of the straight line in this plot is a measure of activation energy for δ' dissolution (122.6 kJ/mol); and the intercept is a measure of the rate constant of the reaction (8.33×10^{10} s^{-1}). The activation energy for a diffusion process involving migration of solute (such as Li or Cu) between the precipitate and the matrix can often be described by the empirical activation energy obtained from Kissinger plots, e.g. in Figure 12.

3.2.2. Alloy 2195

Figure 13 is a DSC thermogram of alloy 2195 (aged at 149°C for 20 hours) scanned at 20°C/min up to 400°C. The precipitation and dissolution reactions important for alloy temper, thermal stability and precipitate distribution considerations in aluminum alloys occur in the RT-350°C range [25]. In Figure 13, there is an endotherm spanning ~ 150 to ~250°C; an exotherm in the ~250 to 290°C range; and an exotherm in the 290 to ~ 330°C. Three samples of alloy 2195 (aged 149°C/20hrs) were individually DSC scanned to temperatures of 210, 230, and 300°C; liquid N_2 quenched, and subsequently analyzed in TEM. These temperatures in the 5°C/min scan correspond to the endotherm and the two exotherms occurring in the 150 to 290°C range in a 20°C/min scan (see Figure 13). Figure 14 (a) and (b) are CDF micrographs of the 210°C quenched sample; Figure 15 (a) and (b) are the BF micrographs of the 300°C quenched sample. Figures 16 (a), (b) and (c) are respectively the [001], [101], and [112] zone axes SAD patterns for the three DSC scanned and quenched samples. An analysis of these micrographs and SAD patterns reveals that the thermal events occurring in the temperature range of 150 to 290°C (in a 20°C/min scan) are complex. The complexity stems from simultaneous dissolution and precipitation reactions which may involve several phases (T_1, δ' and θ'). The following is a summary of the microstructural evolution in the 150-290°C range, based on the TEM analysis.

The microstructure prior to the DSC scan (see Figures 7 and 8) is comprised largely of T_1 with interspersions of small amounts of θ'. The endotherm spanning ~150 to 250°C is largely a result of the dissolution of an appreciable amount of T_1 as can be observed by comparison of Figures 8 and 14(a). In addition, a reduction in intensity of T_1 reflections was observed in the SAD patterns. The exotherm spanning ~250 to 290°C corresponds to re-precipitation of T_1. The re-precipitated T_1 is appreciably coarser as seen in Figure 15 and as also evidenced in Figure 16 by the appearance of three spots along the <111> streaks. Re-precipitation phenomenon under dynamic heating conditions in DSC has been previously reported for under-aged Al-Li alloys [26, 27]. The exotherm spanning 290 to ~330°C appears to be a result of the on-going T_1 dissolution (endothermic reaction) and the simultaneous precipitation of θ' (exothermic reaction). This description of the 290 to

10

~330°C exotherm is based on the DSC characterization of an Al-Cu-Li alloy [25], similar in chemical composition and heat treatment to the alloy 2195 in the present study. The strong T_1 re-precipitation observed in alloy 2195 suggests that the T8 condition still has appreciable supersaturation.

3.3. <u>Overview of strength and toughness of alloys 1460 and 2195</u>

An extensive microstructural characterization of the alloys was presented in the previous sections. A discussion of the influence of the precipitate phases δ' and T_1 on mechanical behavior is presented below.

3.3.1. <u>Alloy 1460</u>

δ' is the dominant strengthening precipitate in alloy 1460. The actual degree of strengthening contributed by δ' is a function of the volume fraction and the size distribution of the particles [28]. During plastic deformation, δ' particles are sheared by dislocations. As δ' has an $L1_2$ structure and is fully coherent with the matrix, the strengthening associated with δ' shearing is largely attributed to order hardening [29]. Strength increases as the resistance to dislocation shearing of δ' increases. However, this mode of deformation can further result in slip localization. Once slip has occurred on a given plane, continued slip on that plane becomes energetically favorable compared to activating slip on an alternate slip system. Persistent planar slip leads to the localization of deformation strains into intense slip bands. Failure may occur by either slip-band fracture, or grain boundary fracture at the intersection of grain boundaries and slip bands due to stress concentrations caused by dislocation pile-ups [29]. As illustrated by the δ'-CDF image in Figure 17, δ' precipitates and, apparently, δ'/Al_3Sc or δ'/Al_3Zr composite particles, are sheared by dislocations during plastic deformation (indicated by arrow heads). The weak beam dark field (WDF) image in Figure 18 shows a large strain contrast which is indicative of a high dislocation density along slip directions on {111} planes. Similarly, the T_1 -CDF image in Figure 19 shows appreciable strain contrast associated with the intense dislocation activity (see the background) at a grain boundary. The

relatively large T_1 precipitates at the boundary are bent and a few small T_1 precipitates are sheared by dislocations (indicated by arrowheads). These observations, which are consistent with behavior reported for other δ' strengthened alloys, suggest that the low toughness in alloy 1460 is associated with the formation of planar slip bands [29]. The grain boundary pinning action of δ'/Al_3Sc composite particles is evident in Figure 20. In the present study, no grain boundary δ' precipitate free zones (PFZ) were observed (see Figure 20) in the alloy 1460.

3.3.2. Alloy 2195

In alloy 2195, T_1 is the dominant strengthening phase. Unlike the ordered, shearable δ' precipitates in alloy 1460 that lead to slip localization, T_1 particles, above a critical size, act as non-shearable obstacles to dislocation motion (relatively small T_1 particles are shearable, as shown in Figure 19) and promote slip homogenization [30]. T_1 exhibits a strong tendency to nucleate heterogeneously on dislocations and low angle grain boundaries. Heterogeneous nucleation sites within a grain are induced by cold work prior to artificial aging, which is used to promote a uniform distribution of heterogeneously nucleated T_1 precipitates. The distributions of T_1 precipitates in the T8 condition are considered responsible for improvements in strength and fracture toughness [31].

4. Summary

A summary of the salient findings on the microstructural characterization of Al-Li alloys 1460 and 2195 is presented here.

* The dominant strengthening precipitates in alloys 1460 and 2195 in the T8 condition are δ' and T_1 respectively.

* Shearable δ' precipitates and extensive slip planarity is associated with poor toughness in many aluminum-lithium alloys and is characteristic of alloy 1460. In contrast, the more homogeneous deformation mode of the T_1 strengthened 2195 may contribute to its superior strength and toughness.

* The alloys 1460 and 2090 have very similar composition and microstructures with

similarities in δ' size distributions and volume fractions. The two alloys appear to have the maximum allowable δ' volume fraction, with no indication of remnant supersaturation. It is therefore unlikely that further strength improvements in them could be effected via alternative heat treatment procedures.

* The alloy 2195 in the T8 condition still has appreciable supersaturation. A pre-age straining treatment which produces a higher density of heterogeneous nucleation sites may result in strength increases.

Acknowledgments

References

1. J.T. Staley, *Aluminum Alloys - Contemporary Research and Applications* (edited by A.K. Vasudevan and R.D. Doherty, Academic Press, Inc.), 31, p.11 (1989).

2. P. E. Bretz and R.R. Sawtell, *Aluminum-Lithium Alloys III* (edited by C. Baker, P.J. Gregson, S.J. Harris, and C.J. Peel, *Inst. of Metals*, London), p.47 (1986).

3. P. E. Bretz and R. G. Gilliland, *Light Metal Age*, 445, p.7 (1987).

4. W.D. Pollock and S.J. Hales, *The 4th International Conference on Aluminum Alloys*, p.358 (1994).

5 . M.S. Domack, C.L. Lach, and J.A. Wagner, *Presentation in AeroMat'96*, (June 6, 1996).

6. X. J. Jiang, Q.H. Gui, Y.Y. Li, L.M. Ma, G.J. Liang, and C.X. Shi, *Scripta. Metall. Mater.*, 29, p.211 (1993).

7. I. N. Fridlyander, A.M. Dritz and T.V. Krymova, *Conference Proceedings of the Aluminium-Lithium-Conference in Garmisch*, p.1245, (1991).

8. I.N. Fridlyander, A.G. Bratukhin, V.G. Davydov, *Conference Proceedings of the Aluminium-Lithium-Conference in Garmisch,* p.35 (1991).

9. N. Blake and M.A. Hopkins, J. Mater. Sci., 20, p. 2861 (1985).

10. L. A. Willey, United States Patent No. 3, 619, p.181 (1971).

11. M.D. Drits, L.S. Toropova, and Yu. G. Bykov: *Metalloved. Term. Obbrab. Met.,* 7, P.60 (1983).

12. V. I. Elagin, V.V. Zakharov, and T.D. Rostova, *Metalloved. Term. Obbrab. Met.,* 7, P. 57 (1983).

13. D.B. Williams and J. W. Edingtion, *Met. Sci.,* 9, p.529 (1975).

14. S. Kang and N.J. Grant, *Metall. Trans.,* 18A, p.2037 (1987).

15. J.C. Huang and A.J. Ardell, *Mat. Sci. and Tech.,* 3, p.176 (1987).

16. K.M. Knowles and W.M. Stobbs, *Acta Cryst.,* B44, p.207 (1988).

17. A.K. Gupta, P. Gaunt and M.S. Chaturvedi, *Phil. Mag.,* 55A, p.375 (1987).

18. I.J. Polmear, *Trans. Metall. Soc. A.I.M.E.* 230, p.1331 (1964).

19. S. Kerry and V. D. Scott, *Metal Sci.,* 18, p.478 (1978).

20. J. M. Papazian, *Metall. Trans.,* 13A, p.761 (1982).

21. R. DeIasi and P. N. Adler, *Metall. Trans.,* 8A, p.1177 (1977).

22. S.W. Chen, C. H. Jan, J. C. Lin, and Y. A. Chang, *Metall. Trans.,* 20A, p. 2247 (1989).

23. Tsung-Rong Chen, Guan-Jye Peng, and J.C. Huang, *Metall. Trans.,* 27A, p.2923 (1996).

24. L.V. Meisel and P.C. Cote, *Acta Metall.,* 31, p.1053 (1983).

25. R.N. Shenoy and J. M. Howe, *Scripta Metall. Mater.,* 33, p.651 (1995).

26. E.S. Balmuth, *Scripta Metall.,* 18, p.301 (1984).

27. R. Nozato and G. Nakai, *Trans. JIM,* 18, p.679 (1977).

28. E. A. Starke, Jr., *Aluminum Alloys - Contemporary Research and Applications* (edited by A.K. Vasudevan and R.D. Doherty, Academic Press, Inc.), 31, p.35 (1989).
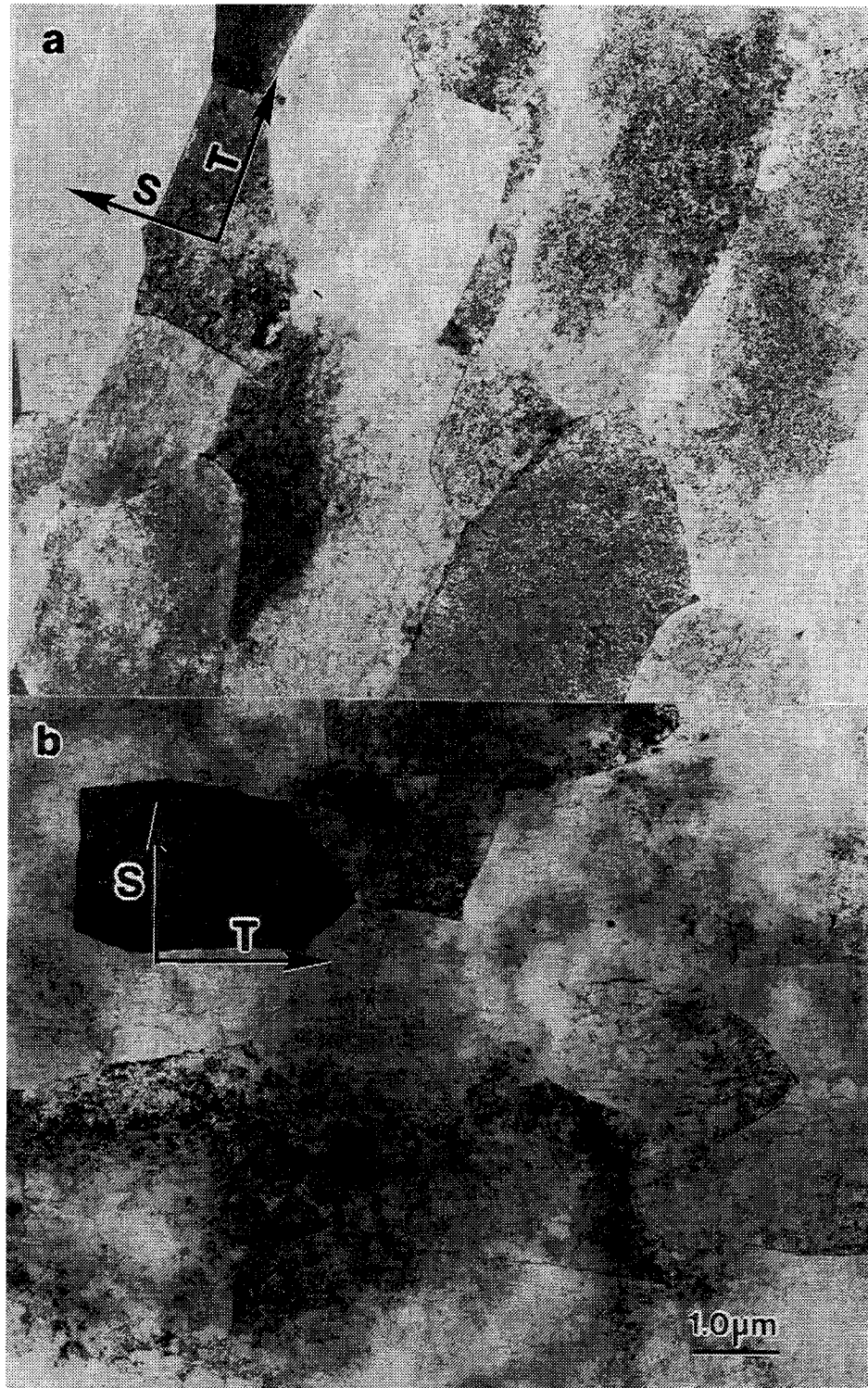
29. J.W. Martin, *Micromechanisms in particle-hardened alloys*, (edited by R.W. Cahn, M.W. Thompson and I.M. Ward, Cambridge University Press, Cambridge, U.K.), p.56 (1980).

30. W.E. Quist and G.H. Narayanan, *Aluminum Alloys - Contemporary Research and Applications* (edited by A.K. Vasudevan and R.D. Doherty, Academic Press, Inc.), 31, p.219 (1989).

Figure 1. TEM micrographs illustrating grain morphology and orientation relative to short and long transverse directions (extrusion direction is normal to micrograph), aged for 20h at 160°C. (a) 1460; (b) 2090.
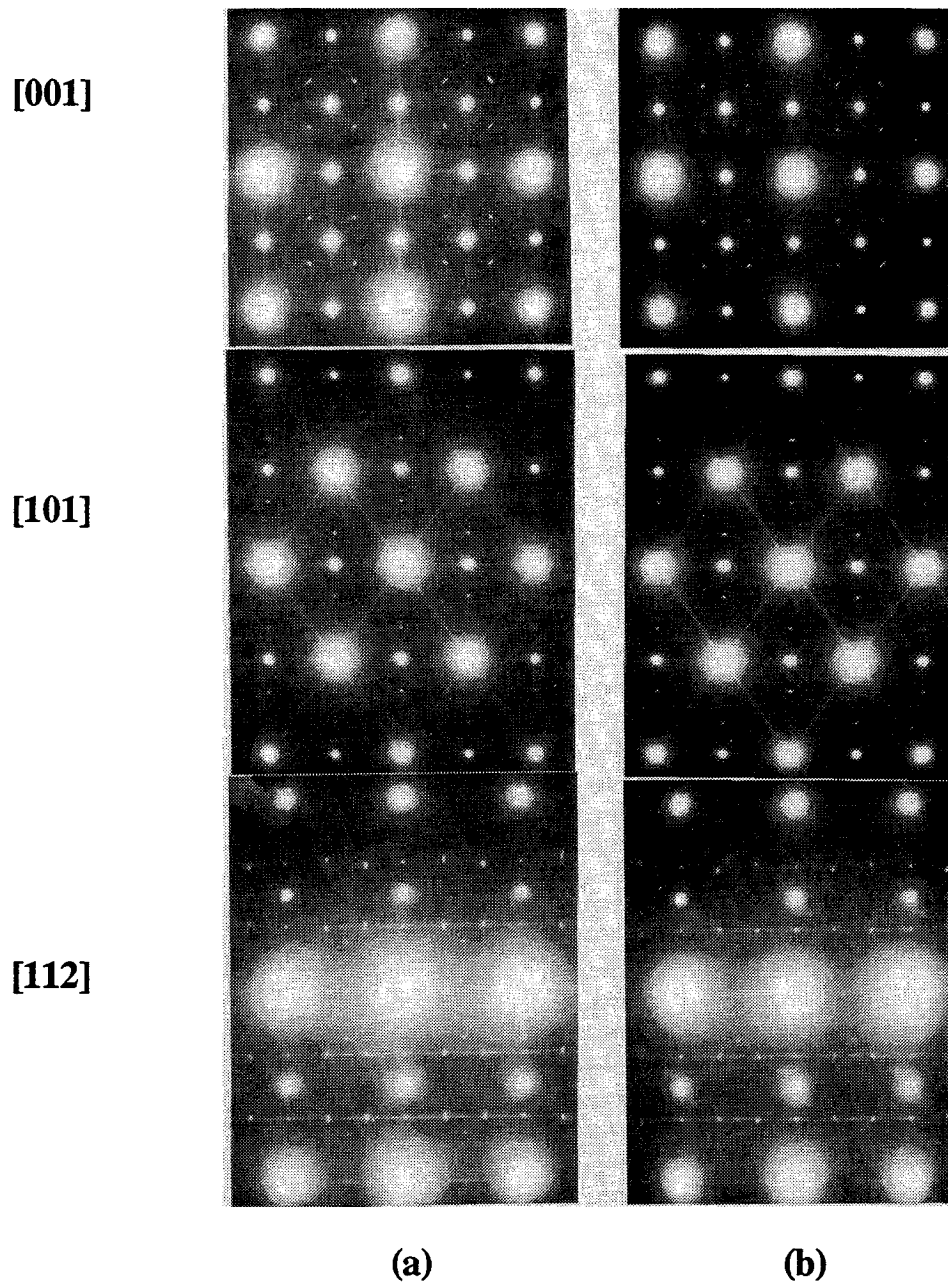
Figure 2. SAD patterns, [001], [101] and [112] zone axes; showing contributions of δ′, T$_1$, θ′ and Ω precipitates, aged for 20h at 160°C. (a)1460; (b) 2090.
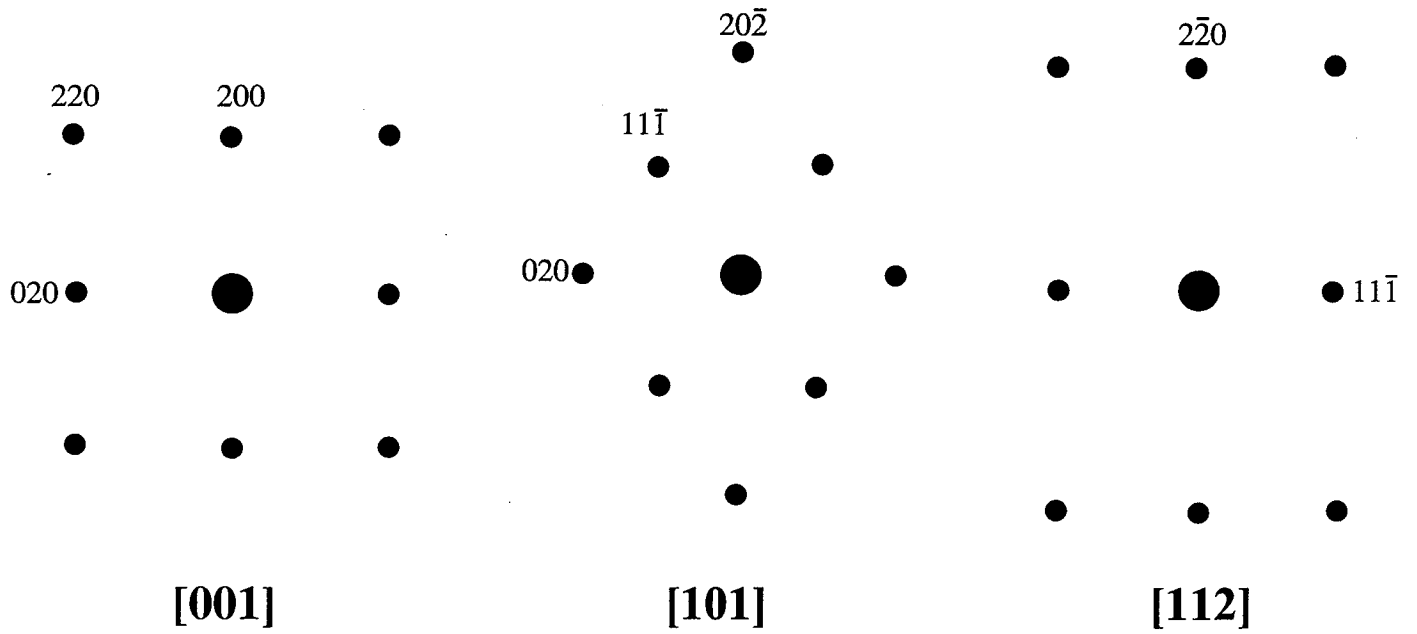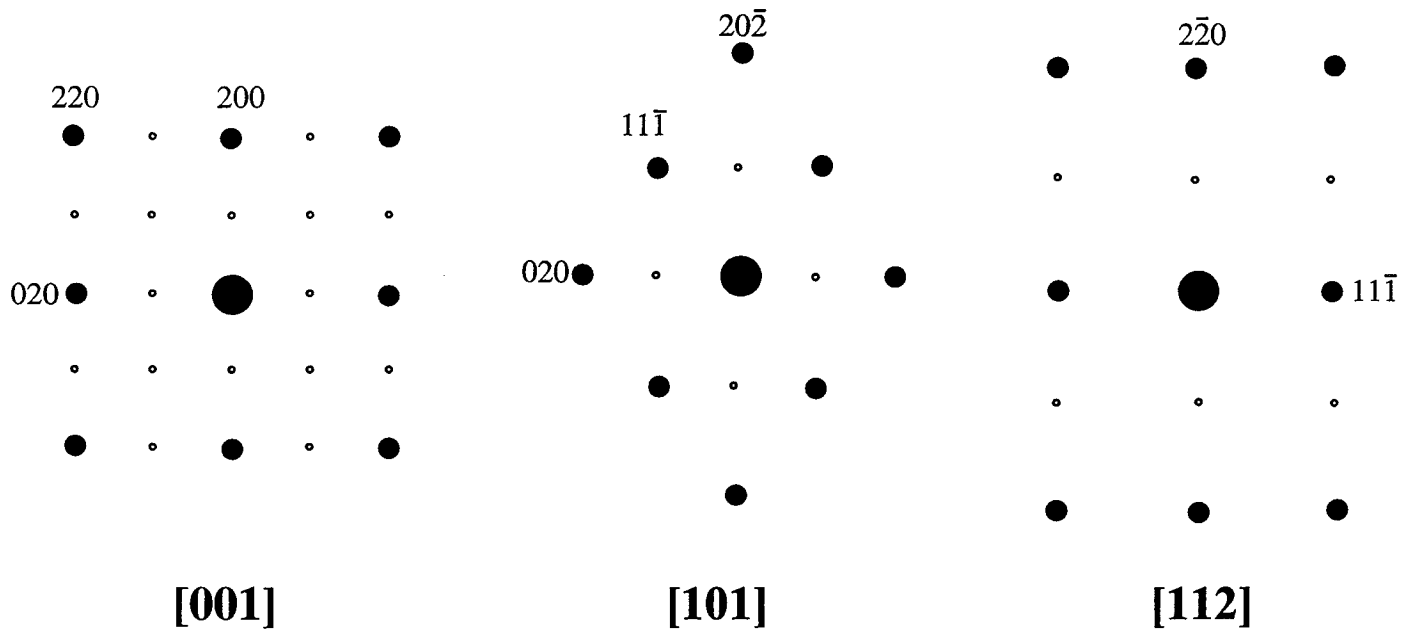
**Figure 3.1.** Schematic of SAD patterns from major zone axes in Al-Li-Cu alloys: (a) The Al matrix; (b) The Al matrix pluse $L1_2$ precipitates.
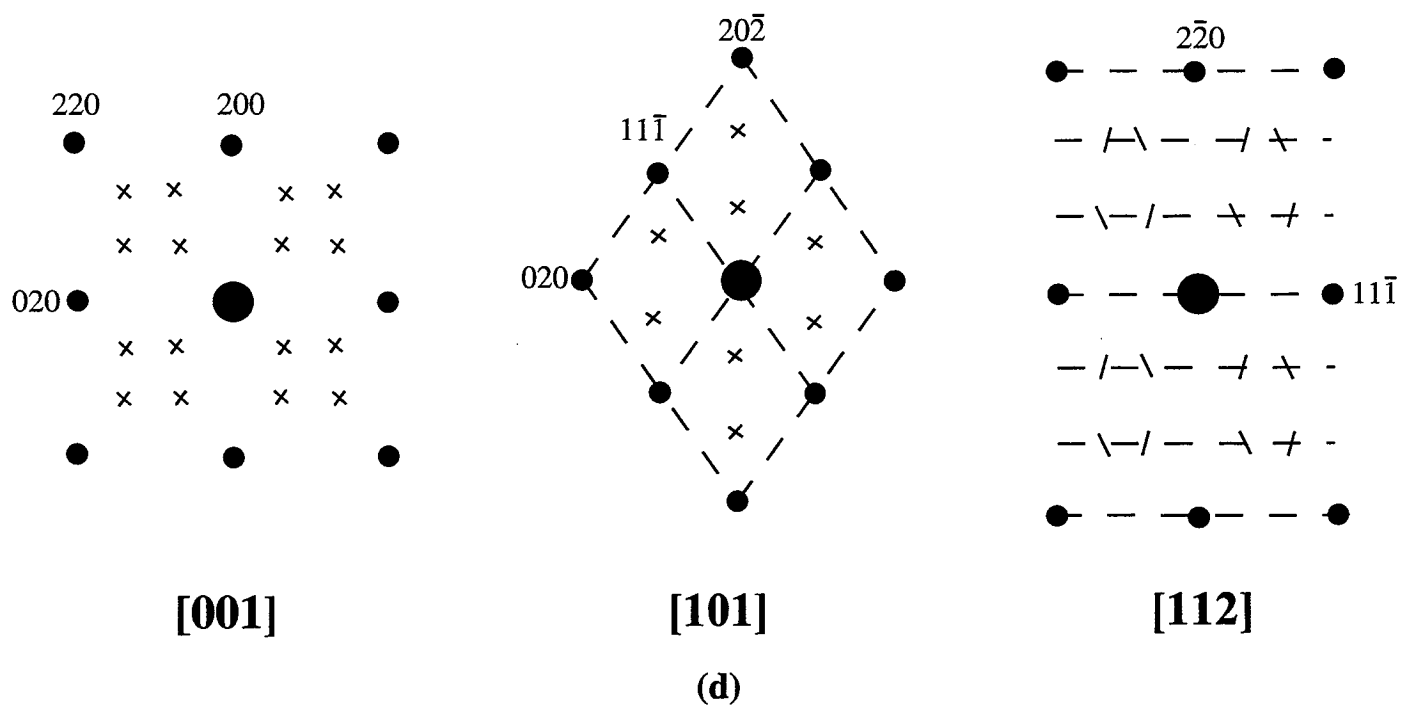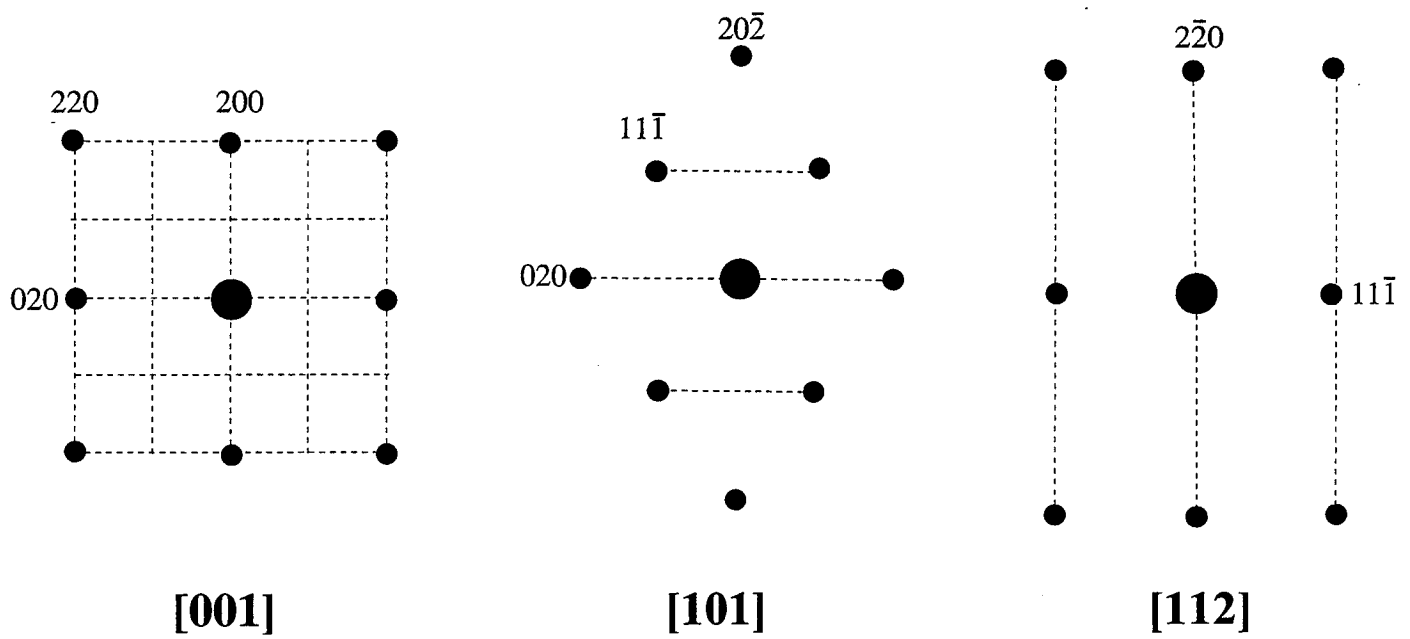
Figure 3.2 Schematic of SAD patterns from major zone axes in Al-Li-Cu alloys: (c) The Al-matrix plus θ' precipitate; (d) The Al-matrix plus T₁ precipitate.
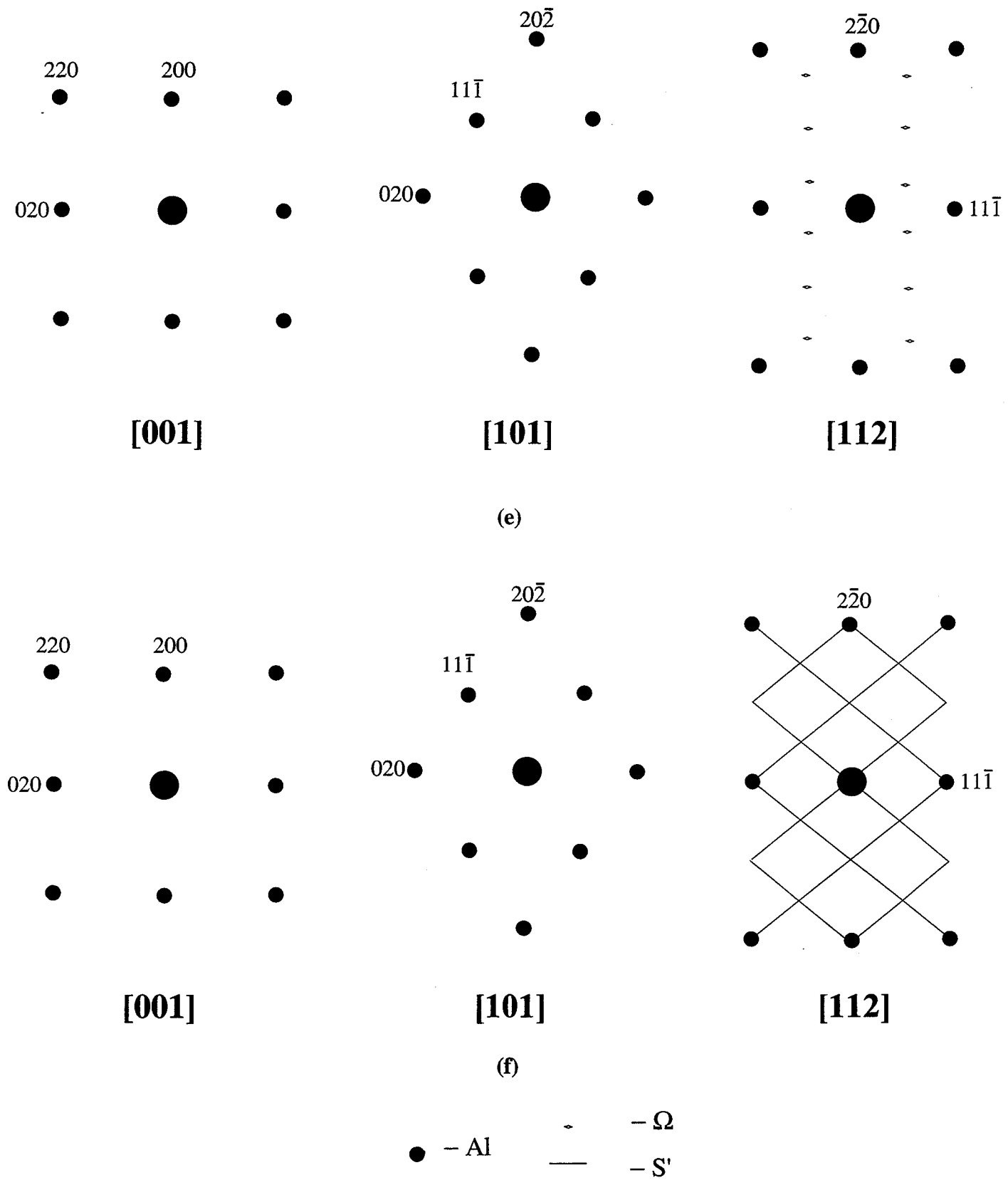
Figure 3.3. Schematic of SAD patterns from major zone axes in Al-Li-Cu alloys: (e) The Al-matrix plus Ω precipitate; (f) The Al-matrix plus S' precipitate.
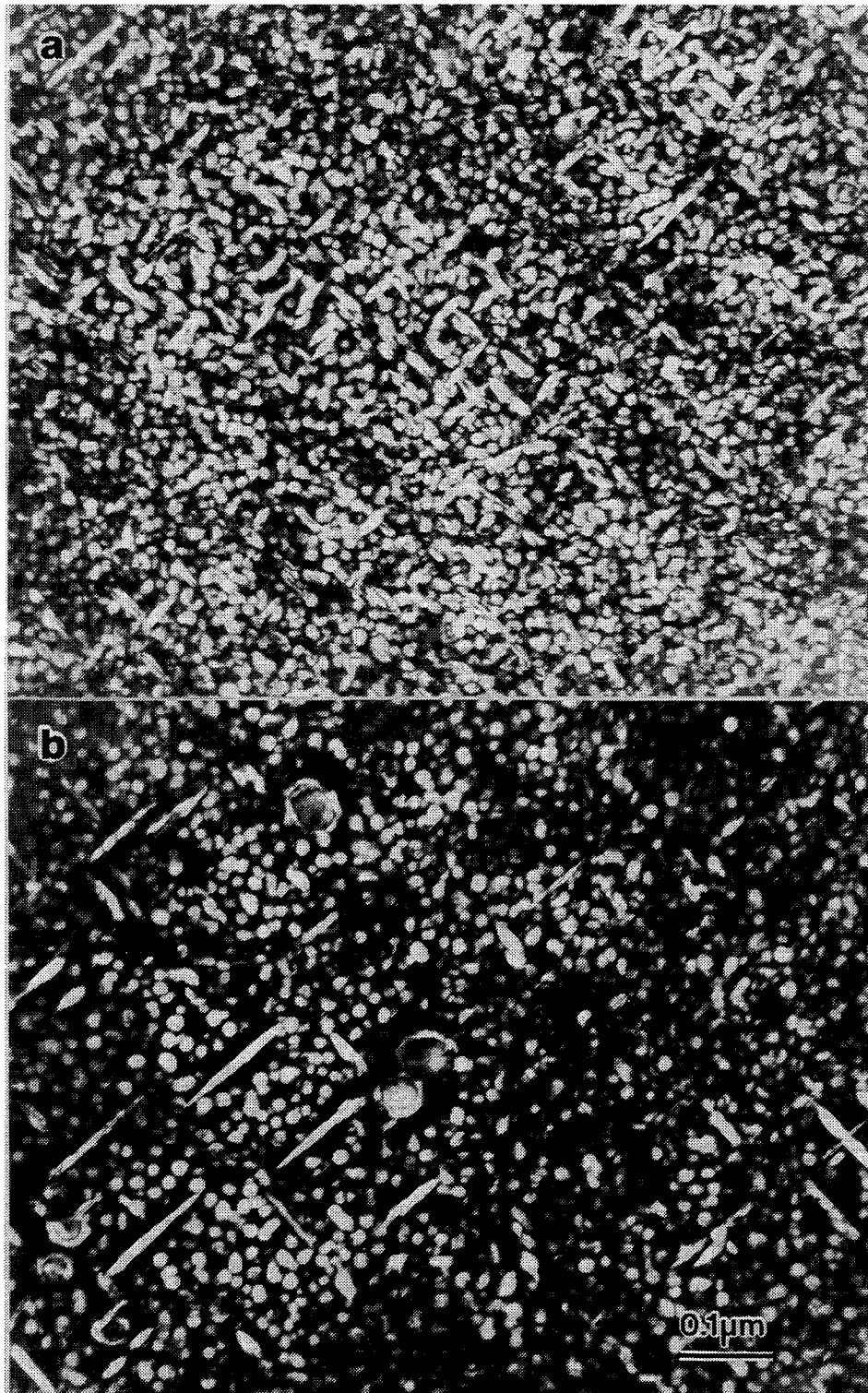
Figure 4. δ′-CDF images from (100) superlattice spots, aged for 20h at 160°C. (a) 1460; (b) 2090.

21
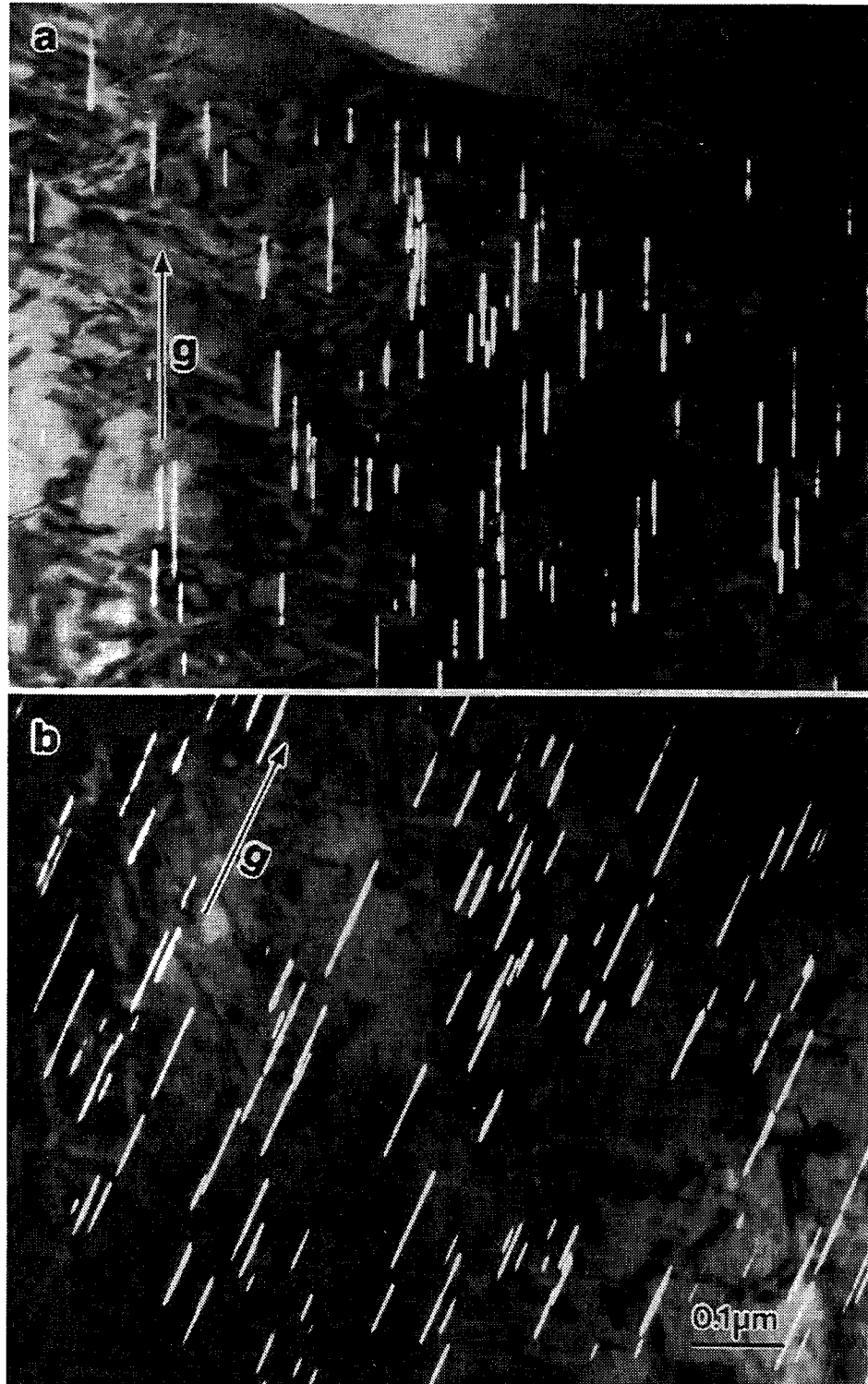
Figure 5. T_1 – CDF images of alloys (a) 1460 and (b) 2090 with **g**=[-111] close to **B**=[101], illustrating the particle size distribution and number density of one variant of T_1 after aging for 20h at 160°C.
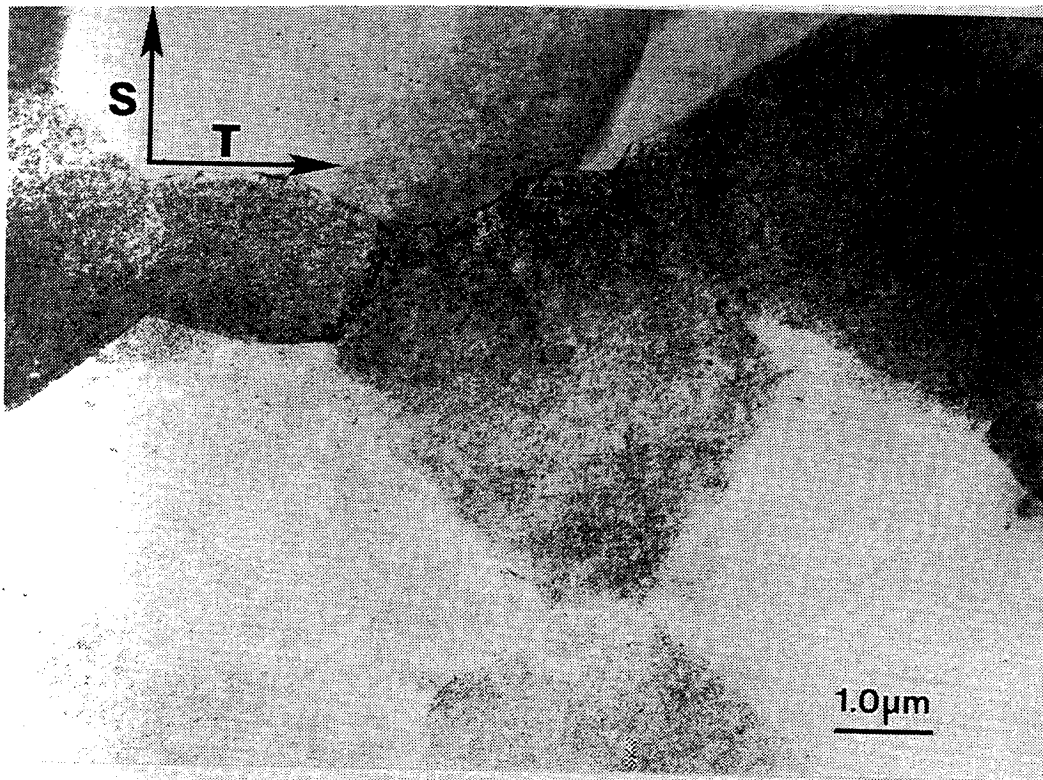
Figure 6. TEM micrographs illustrating grain morphology and orientation relative to short and long transverse directions (extrusion direction is normal to micrograph), 2195, aged for 15h at 149°C.

[001]   **[101]**   **[112]**
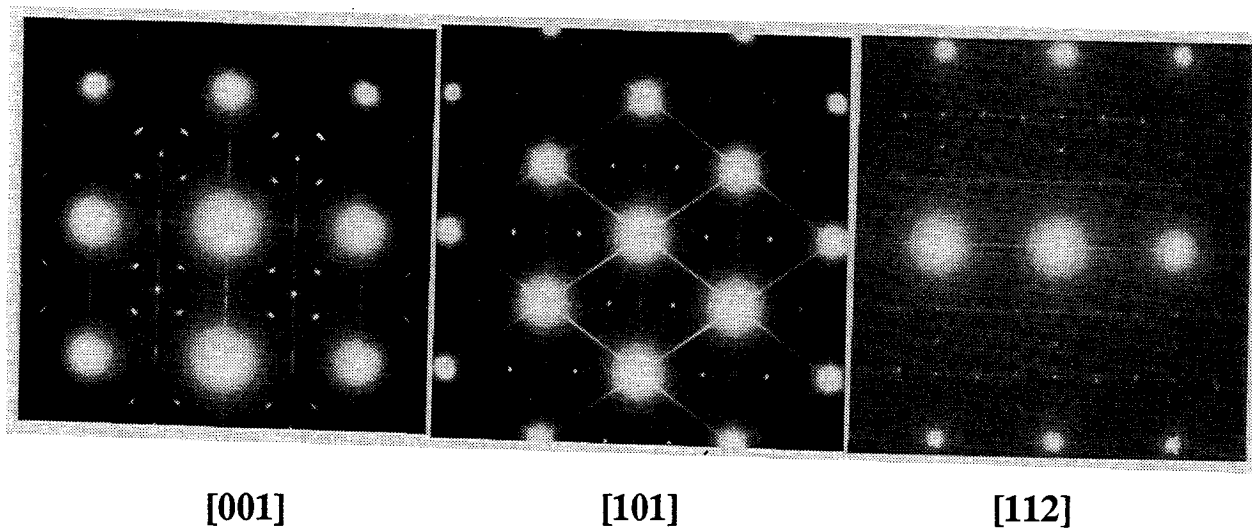
Figure 7. SAD patterns, [001], [101] and [112] zone axes of alloy 2195, aged for 15h at 149°C.
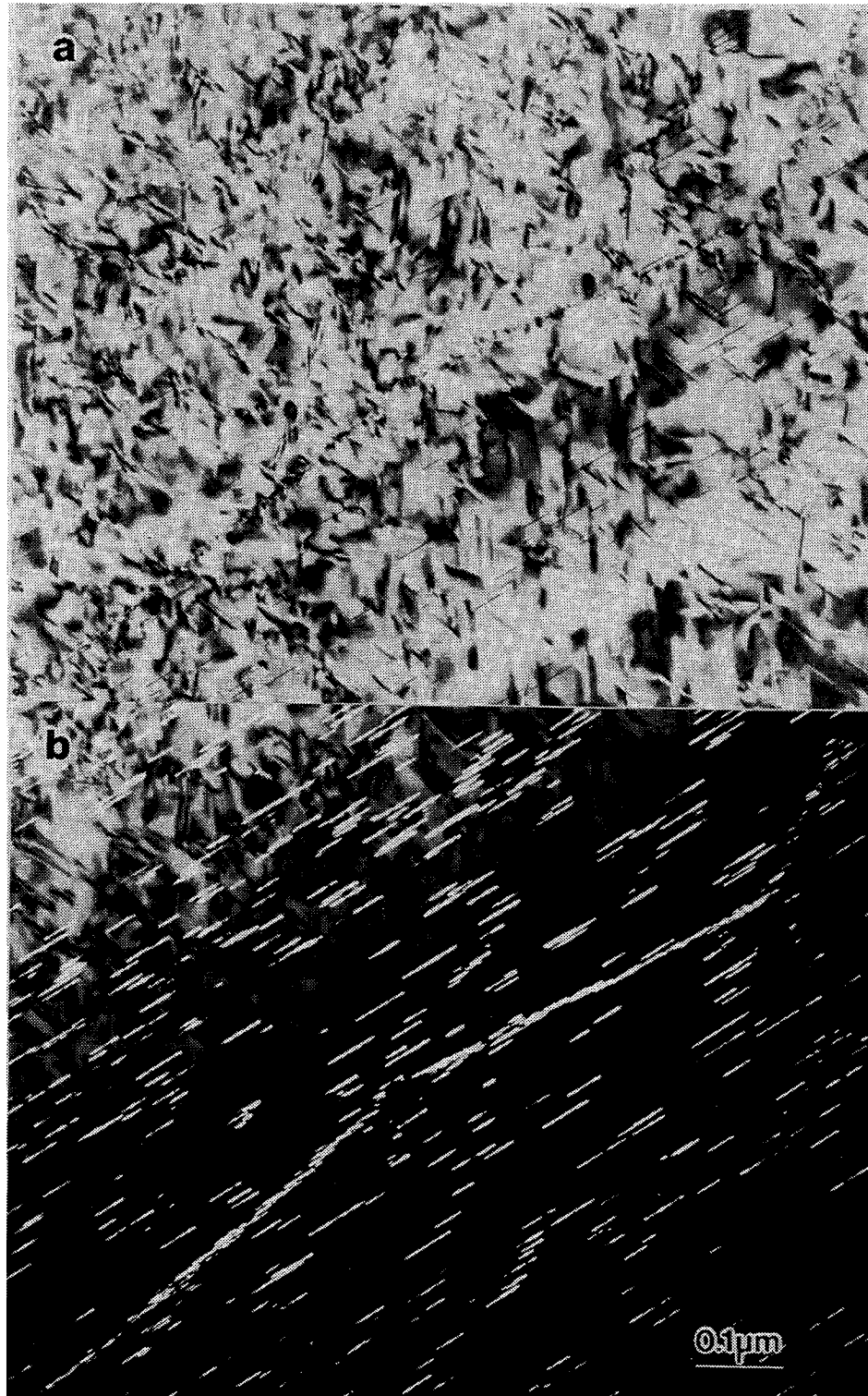
Figure 8. TEM images showing distribution of T_1 precipitates within the matrix, and on a subgrain boundary in alloy 2195, aged for 15h at 149°C. (a) BF; (b) T_1 - CDF.
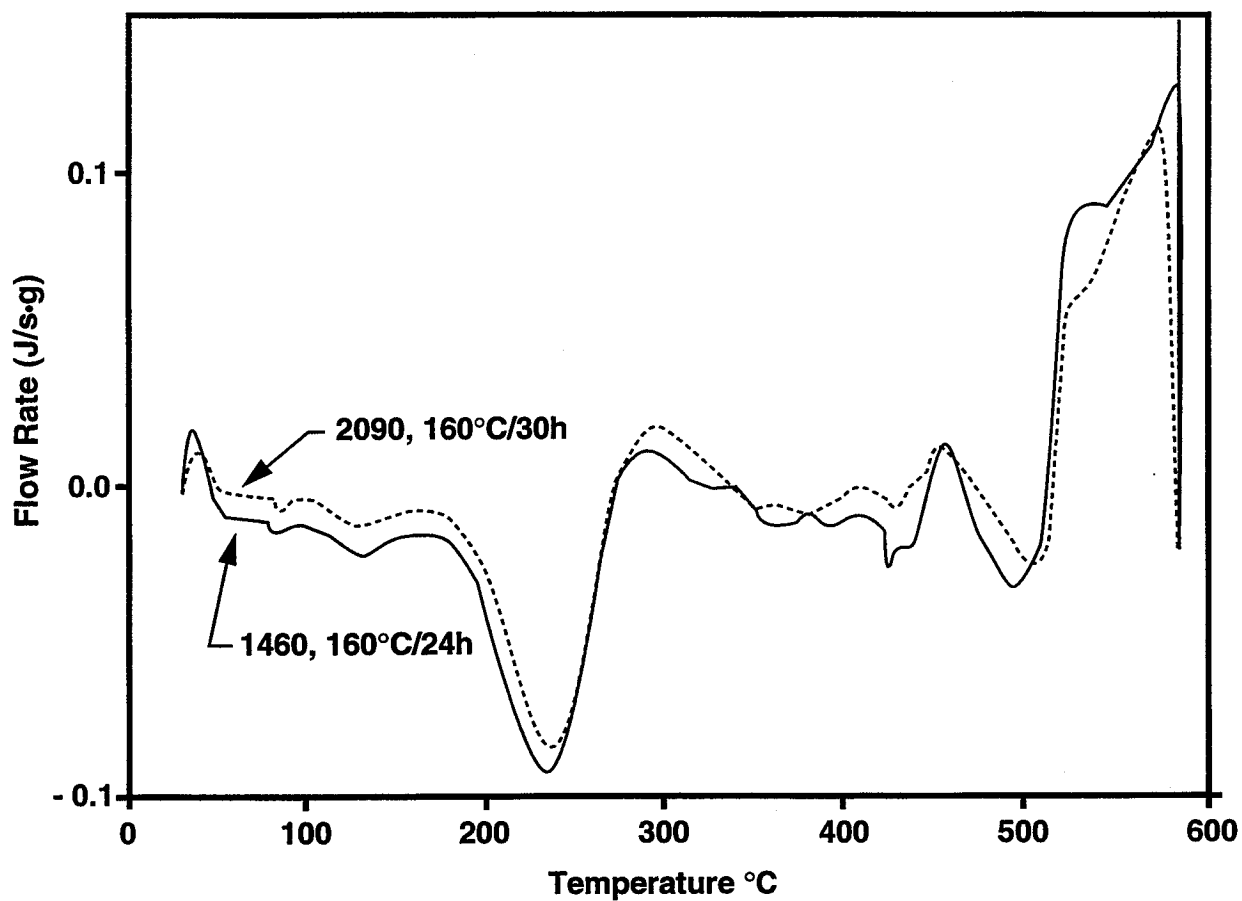
Figure 9. DSC signatures of alloys 1460 (aged for 24 h at 160°C) and 2090 aged for 30 h at 160°C), at 20°C/min scanning rate.
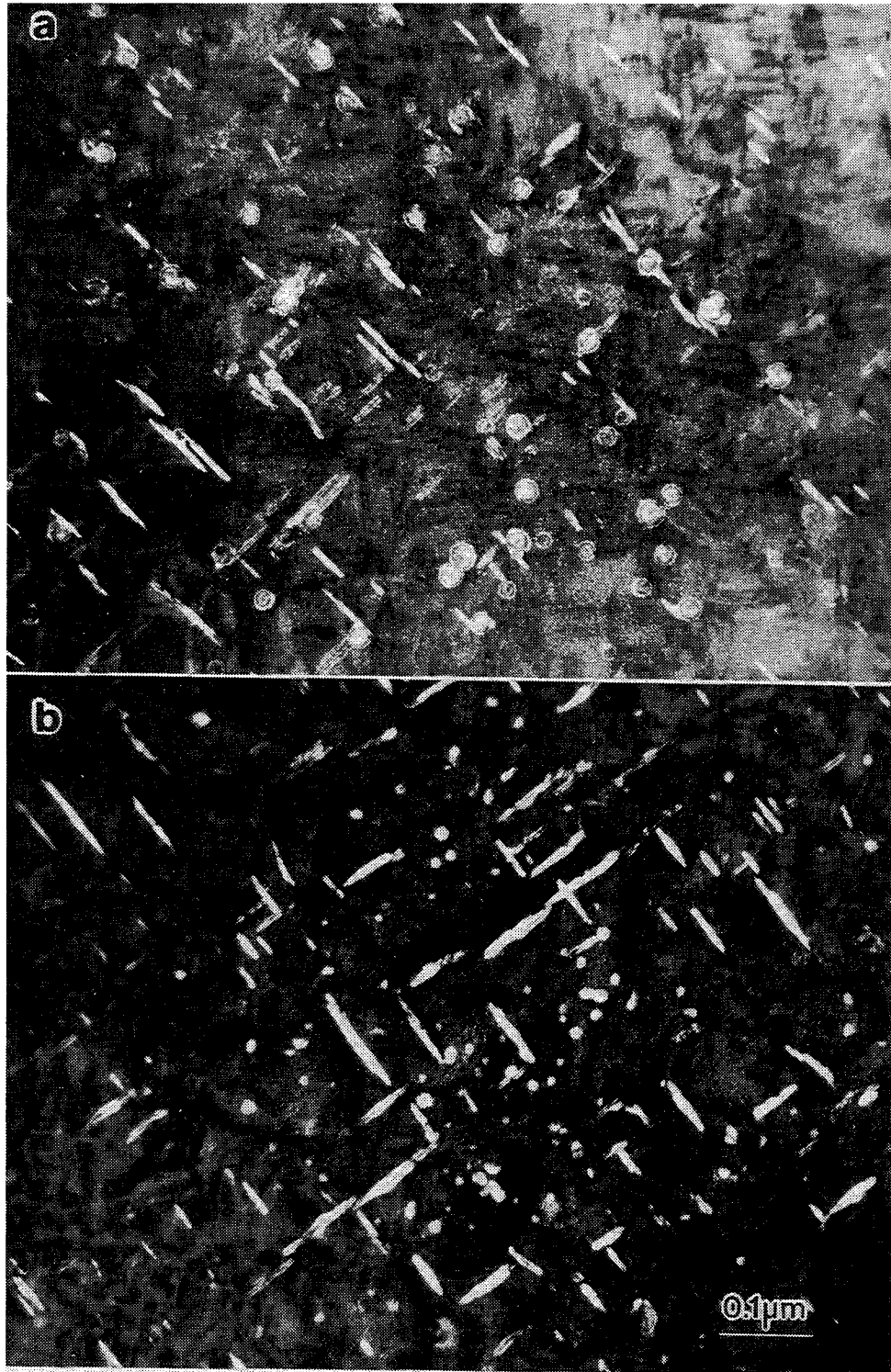
Figure 10. δ' - CDF images of samples DSC scanned up to 245°C and liquid N₂ quenched. (a) 1460, initially aged for 24h at 160°C; (b) 2090, initially aged for 30h at 160°C.
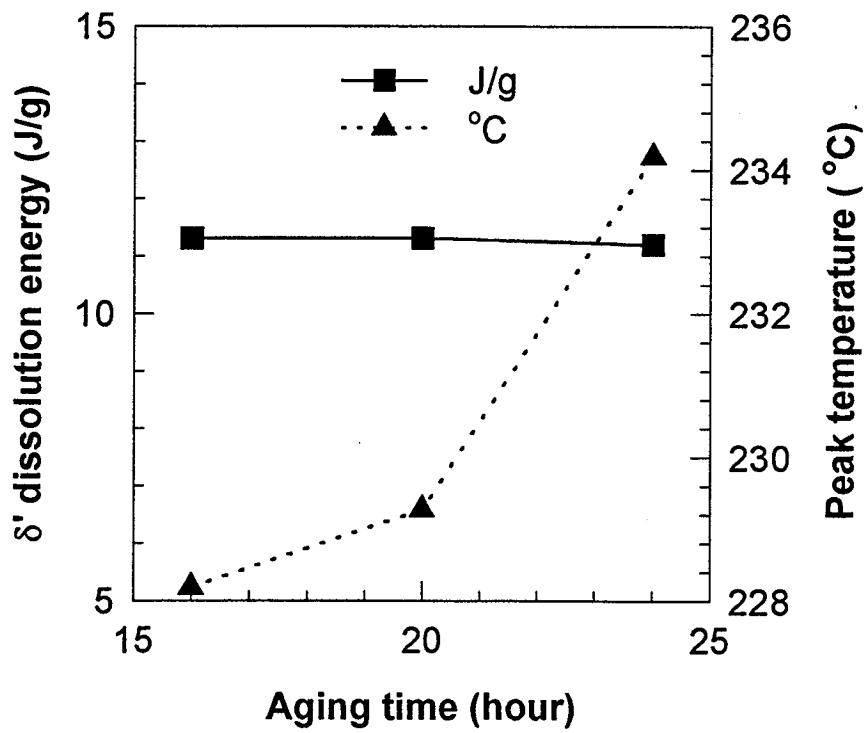
Figure 11. Area under the curve and peak temperature of δ' dissolution enotherm in alloy 1460, as a function of aging time at the aging temperature of 160 °C.
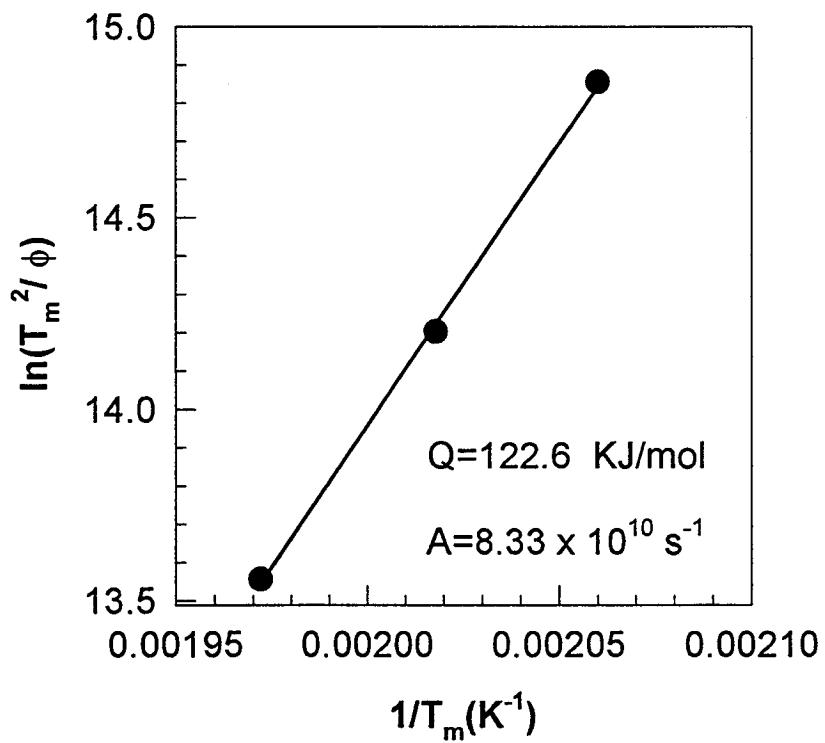
Figure 12. Kissinger plot for δ' dissolution in alloy 1460, aged for 24 h at 160°C.
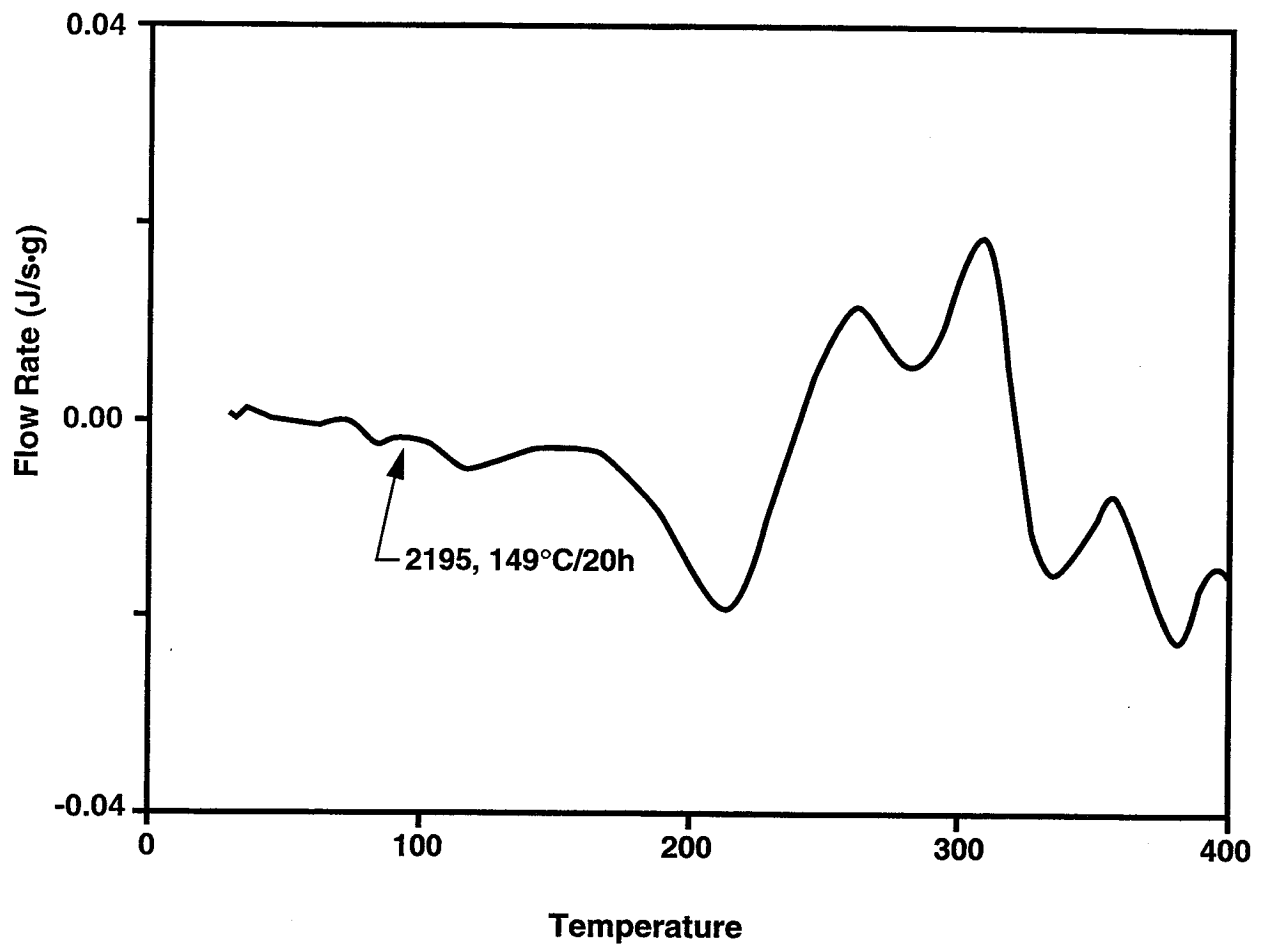
Figure 13. DSC signature of alloy 2195, aged for 20h at 149°C, at 20°C/min scanning rate.
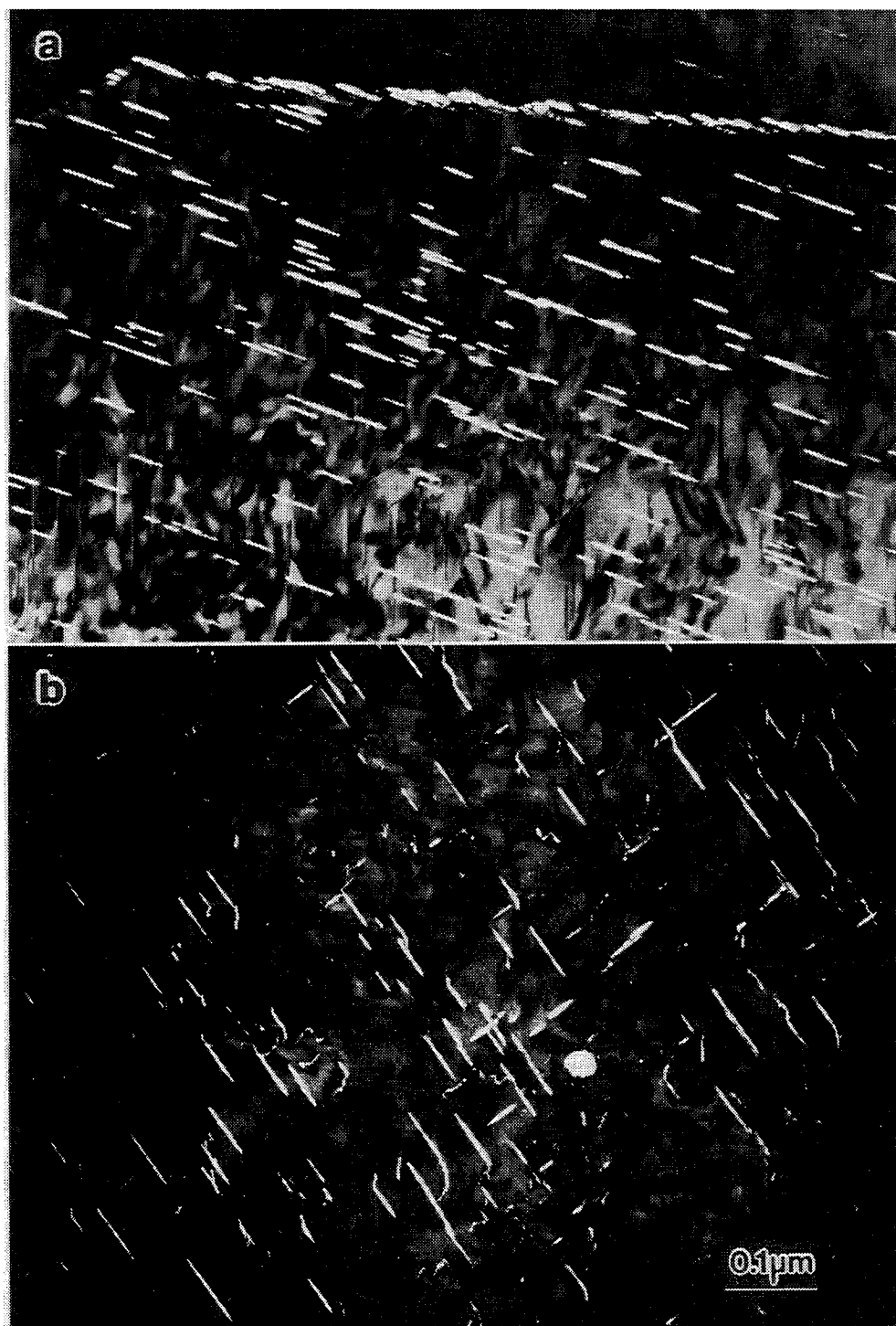
Figure 14. TEM micrographs of 2195, initially aged for 20 h at 149 °C, DSC scanned up to 210°C and liquid N_2 quenched. (a) T_1 -CDF; (b) θ' - CDF .

Figure 15. TEM BF images of 2195, aged for 15h at 149°C, DSC scanned up to 300°C and liquid N_2 quenched. (a) g=[-111], near B=[101]; (b) B=[101].
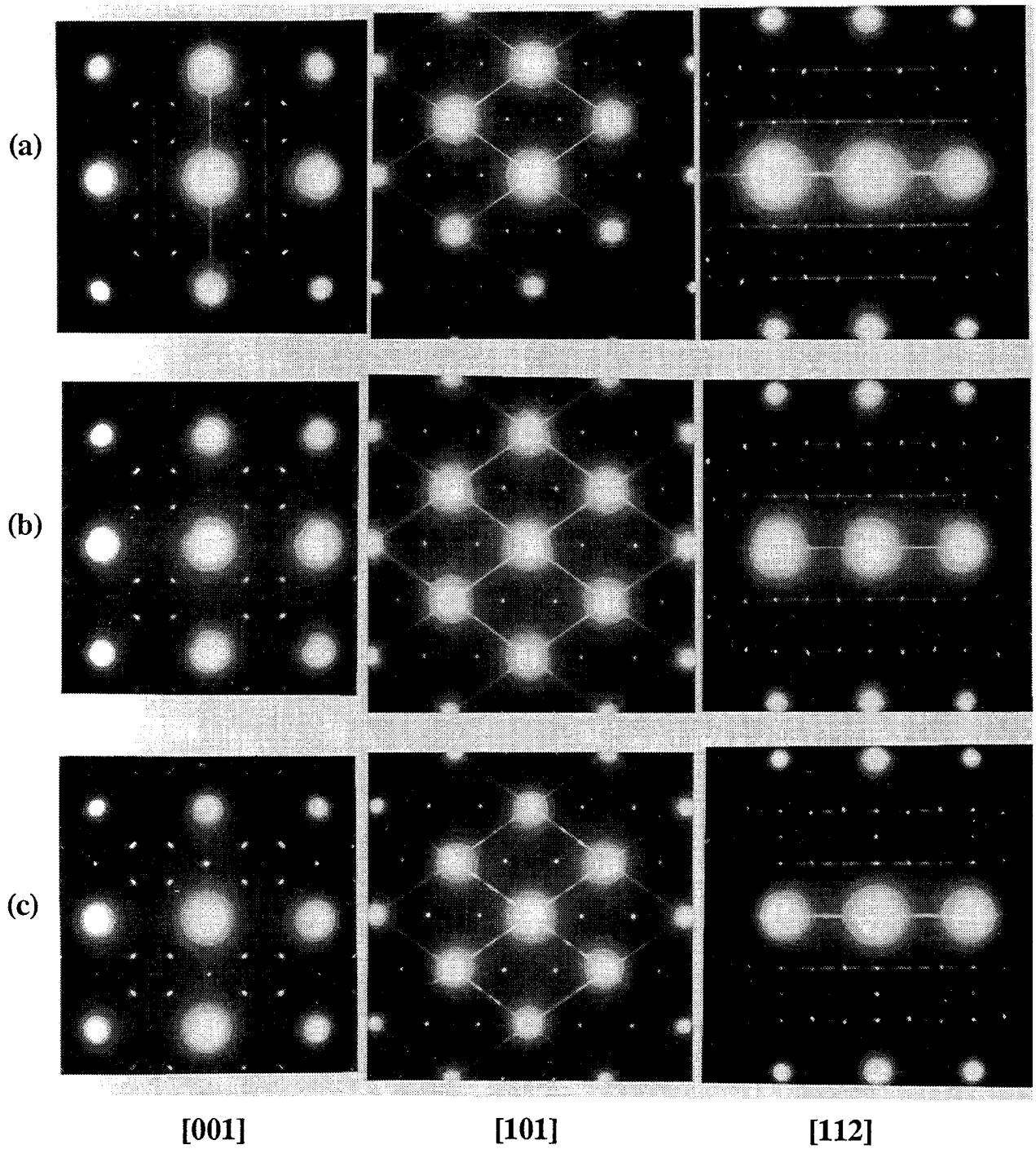
Figure 16. [001], [101] and [112] SAD patterns of alloy 2195, aged for 15 h at 149°C. Quenched in liquid N_2 after DSC scans up to: (a) 210°C; (b) 230°C; (c) 300°C.
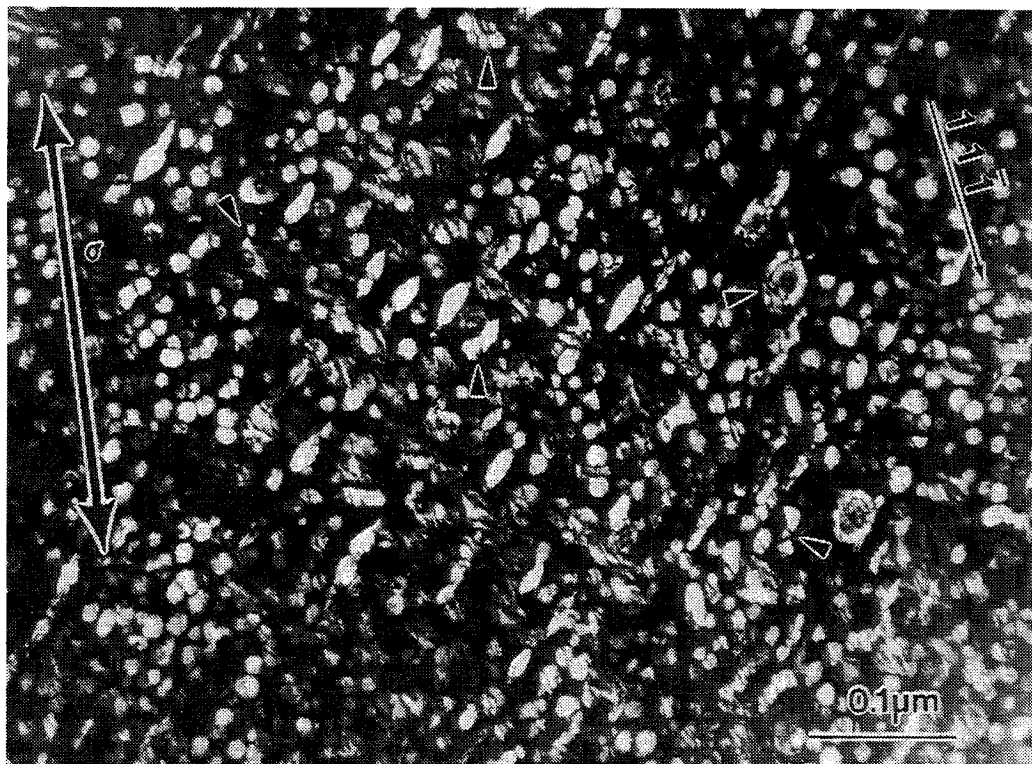
Figure 17. δ′ − CDF image of a thin foil from a fractured tensile sample of alloy 1460, aged for 20h at 160°C. The double arrow indicates the direction of tensile stress σ.
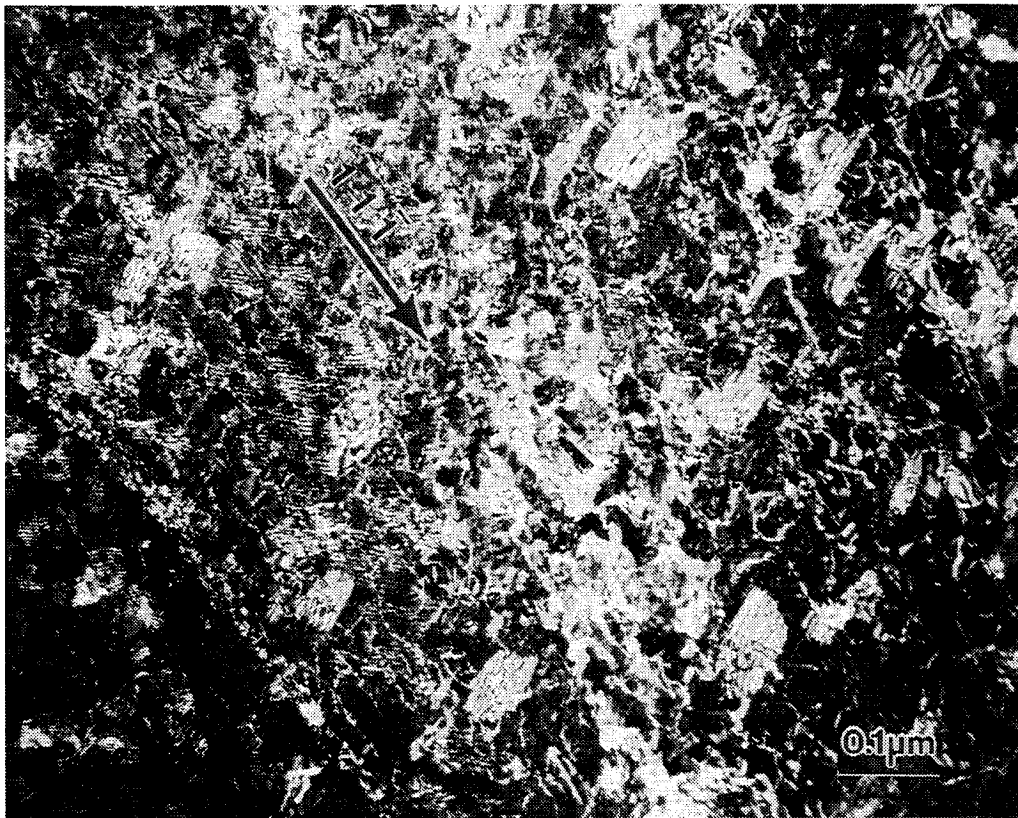
Figure 18. Weak-beam dark-field image of a thin foil from a fractured tensile sample of alloy 1460, aged for 20h at 160°C.
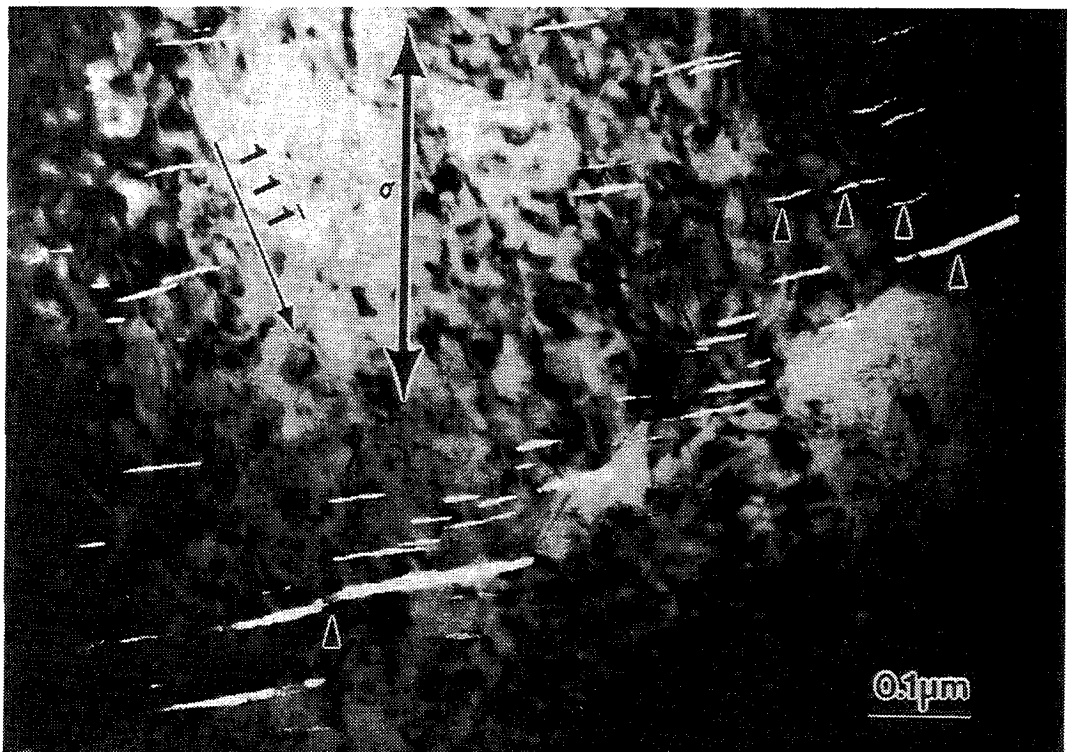
Figure 19. T_1 – CDF image of a thin foil from a fractured tensile sample of alloy 1460, aged for 20h at 160°C. T_1 plates at the boundary are bent and a few small T_1 plates near the boundary are sheared by dislocations (indicated by arrowheads). The double arrow indicates the direction of tensile stress σ.

REPORT DOCUMENTATION PAGE

Public reporting burden for this collection of information is estimated to average 1 hour per response, including the time for reviewing instructions, searching existing data sources, gathering and maintaining the data needed, and completing and reviewing the collection of information. Send comments regarding this burden estimate or any other aspect of this collection of information, including suggestions for reducing this burden, to Washington Headquarters Services, Directorate for Information Operations and Reports, 1215 Jefferson Davis Highway, Suite 1204, Arlington, VA 22202-4302, and to the Office of Management and Budget, Paperwork Reduction Project (0704-0188), Washington, DC 20503.

1. AGENCY USE ONLY (Leave blank)	2. REPORT DATE February 1998	3. REPORT TYPE AND DATES COVERED Contractor Report

4. TITLE AND SUBTITLE
Microstructural Characterization of Aluminum-Lithium Alloys 1460 and 2195

6. AUTHOR(S)
Z. M. Wang and R. N. Shenoy

5. FUNDING NUMBERS
NAS1-96014

WU 242-20-05-05

7. PERFORMING ORGANIZATION NAME(S) AND ADDRESS(ES)
Analytical Services & Materials, Inc.
Hampton, VA 23666

8. PERFORMING ORGANIZATION REPORT NUMBER

9. SPONSORING/MONITORING AGENCY NAME(S) AND ADDRESS(ES)

National Aeronautics and Space Administration
Langley Research Center
Hampton, VA 23681-2199

10. SPONSORING/MONITORING AGENCY REPORT NUMBER
NASA/CR-1998-206914

11. SUPPLEMENTARY NOTES
Langley Technical Monitor: John Wagner

12a. DISTRIBUTION/AVAILABILITY STATEMENT

Unclassified–Unlimited
Subject Category 26   Distribution: Standard
Availability: NASA CASI (301) 621-0390

12b. DISTRIBUTION CODE

13. ABSTRACT (Maximum 200 words)
Transmission electron microscopy (TEM) and differential scanning calorimetry (DSC) techniques were employed to characterize the precipitate distributions in lithium-containing aluminum alloys 1460 and 2195 in the T8 condition. TEM examinations revealed delta prime and T1 as the primary strengthening precipitates in alloys 1460 and 2195 respectively. TEM results showed a close similarity of the Russian alloy 1460 to the U.S. alloy 2090, which has a similar composition and heat treatment schedule. DSC analyses also indicate a comparable delta prime volume fraction. TEM study of a fractured tensile sample of alloy 1460 showed that delta prime precipitates are sheared by dislocations during plastic deformation and that intense stress fields arise at grain boundaries due to planar slip. Differences in fracture toughness of alloys 1460 and 2195 are rationalized on the basis of a literature review and observations from the present study.

14. SUBJECT TERMS
Al-Cu-Li Alloys, Transmission electron microscopy (TEM)
Differential scanning calorimetric (DSC), microstructure

15. NUMBER OF PAGES
46

16. PRICE CODE
A03

17. SECURITY CLASSIFICATION OF REPORT	18. SECURITY CLASSIFICATION OF THIS PAGE	19. SECURITY CLASSIFICATION OF ABSTRACT	20. LIMITATION OF ABSTRACT
Unclassified	Unclassified	Unclassified	

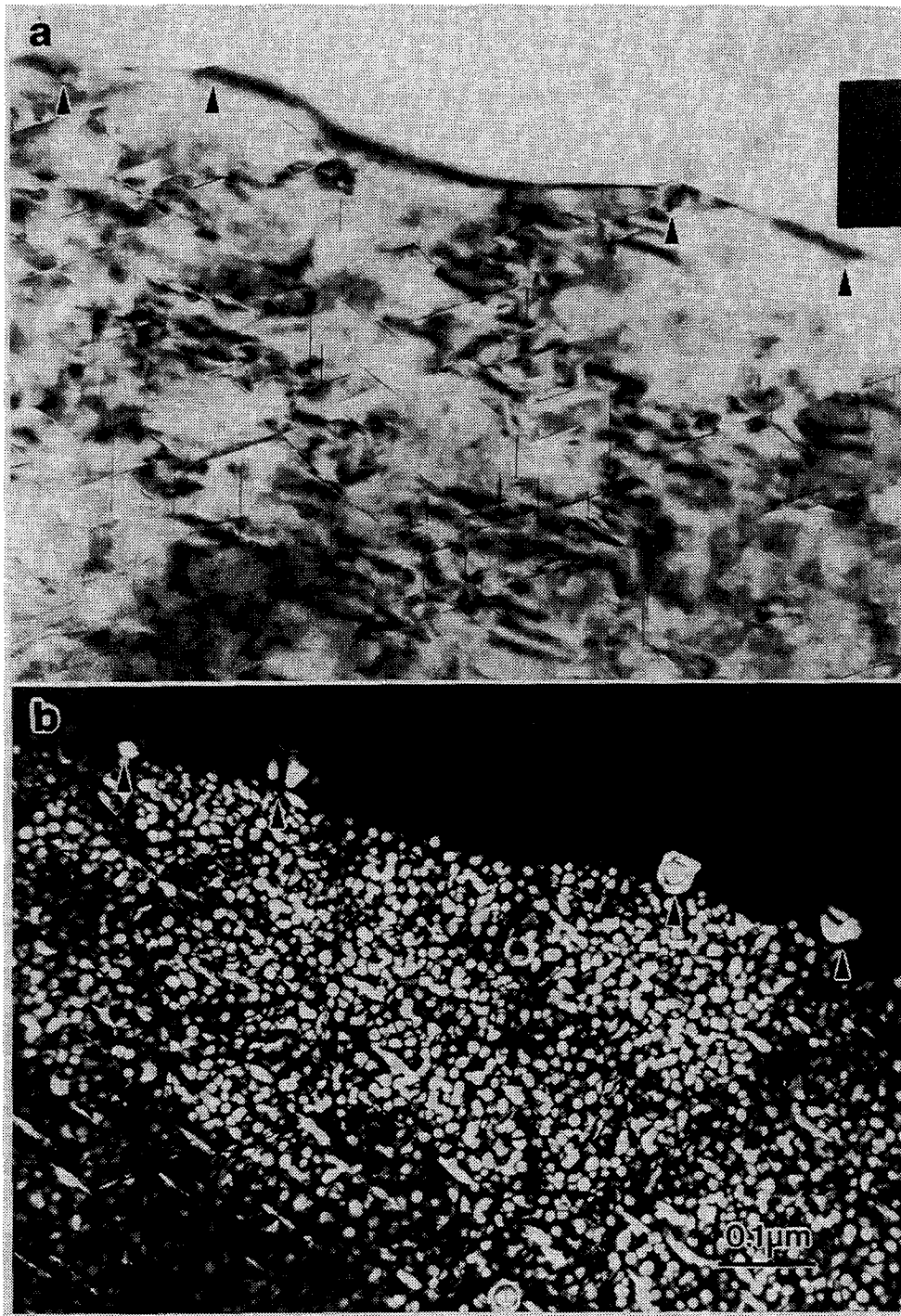**Figure 20.** TEM micrographs of alloy 1460, aged for 20h at 160°C, illustrating δ'/Al_3Sc composite particles (indicated by arrowheads) pinning a grain boundary. (a) BF (b) δ' - CDF.